Supporting Information

Photomechanically accelerated degradation of perovskite solar cells

Haonan Wang,[a] Qing Li,[a] Yan Zhu,[a] Xinyuan Sui,[a] Xiulian Fan,[c] Miaoyu Lin,[a] Yifeng Shi,[d] Yichu Zheng,[e] Haiyang Yuan,[a] Yu Zhou,[c] Haibao Jin,*[b] Hua Gui Yang,[a] Yu Hou*[a] and Shuang Yang*[a]

[a] Key Laboratory for Ultrafine Materials of Ministry of Education, Shanghai Engineering Research Center of Hierarchical Nanomaterials, School of Materials Science and Engineering, East China University of Science and Technology; 200237, Shanghai, China. E-mail: yhou@ecust.edu.cn; syang@ecust.edu.cn

[b] Shanghai Key Laboratory of Advanced Polymeric Materials, Frontiers Science Center for Materiobiology and Dynamic Chemistry, School of Materials Science and Engineering, East China University of Science and Technology; 200237, Shanghai, China. E-mail: haibaojin@ecust.edu.cn

[c] Hunan Key Laboratory of Nanophotonics and Devices, School of Physics, Central South University; Changsha, Hunan 410083, P. R. China

[d] Key Laboratory of Materials for High-Power Laser, Shanghai Institute of Optics and Fine Mechanics, Chinese Academy of Sciences; 201800, Shanghai, China

[e] School of Mechatronic Engineering and Automation, Shanghai University, Shanghai 200444, China

Experimental Section

Materials

Cesium iodide (CsI, 99.9%), poly(bis(4-phenyl)(2,4,6-trimethylphenyl)amine) (PTAA, average GPC Mn 7000-10000), poly(3-hexylthiophene) (P3HT), dimethyl sulfoxide (DMSO, 99.9%), N,N-dimethylformamide (DMF, 99.8%), chlorobenzene (CB, 99.8%), isopropanol (IPA, 99.5%), were purchased from Sigma Aldrich. Methylammonium iodide (MAI), methylammonium bromide (MABr) and formamidinium iodide (FAI) were purchased from Greatcell Solar Materials. Lead iodide (PbI_2, 99.99%) and lead bromide ($PbBr_2$, 99.9%) were purchased from Energy Chemical. Ethanol (AR, 99.7%) were purchased from General-Reagent. [6,6]-phenyl-C61-butyric acid methyl ester ($PC_{61}BM$, 99.5%) and bathocuproine (BCP, 99%) were purchased from Nichem chemicals. [2-(3,6-Dimethyl-9H-carbazol-9yl)butyl]phosphonic acid (MeO-2PACz) was purchased from TCI. Methylammonium chloride (MACl, 99.5%) was purchased from Xi'an Polymer Light Technology Corp. Trans-polyisoprene (TPI, 99%, the average molecular weight is 180,000) was purchased from Shanghai Titan Scientific Co., Ltd. Indium tin oxide (ITO) glass substrates (15 $\Omega \cdot sq^{-1}$) were purchased from Advanced Election Technology Co., Ltd. All the materials were stored in a nitrogen-filled glove box and used directly as received without any further purification.

Device fabrication

Solar cells were fabricated with a p-i-n heterojunction configuration (ITO/ MeO-2PACz /perovskite/$PC_{61}BM$/BCP/Ag). Patterned ITO glass substrates were cleaned with soap, water, and ethanol under ultrasonication and then treated with ultraviolet ozone for 30 min. The hole transport layer was prepared by spin-coating 0.3 mg mL^{-1} MeO-2PACz

ethanol solution at 3000 rpm for 30 s and then annealed at 100 °C for 10 min. After the deposition of perovskite films, 20 mg mL^{-1} $PC_{61}BM$ chlorobenzene and 0.5 mg mL^{-1} BCP ethanol solutions were spin-coated at 2000 rpm for 45 s and 4000 rpm for 45 s, respectively. Finally, 100 nm of Ag was thermally evaporated as the back electrode.

For $Cs_{0.05}FA_{0.81}MA_{0.14}PbI_{2.85}Br_{0.15}$ film, 1.5M precursor solution was prepared by dissolving CsI, MABr, FAI, $PbBr_2$, and PbI_2 in mixed solvents of DMSO and DMF (v:v = 1:4) with a chemical formula of $Cs_{0.05}FA_{0.81}MA_{0.14}PbI_{2.85}Br_{0.15}$. The TPI was incorporated into the perovskite precursor solution, then stirred for 12 h at 60 °C, and the solution was filtered with 0.22 μm polytetrafluoroethylene (PTFE) membrane before fabricating perovskite film. The perovskite film was prepared by spin-coating at 1000 rpm for 5 s and 4000 rpm for 20 s, and 150 μL CB was dropped at 20 s during spinning, followed by annealing at 40 °C for 30 min and 100 °C for 30 min.

For $Cs_{0.1}FA_{0.9}PbI_3$ film, 1.5 M precursor solution was prepared by dissolving PbI_2, FAI, CsI, and 15 mol% MACl in mixed solvents of DMSO and DMF (v:v = 1:3) with a chemical formula of $Cs_{0.1}FA_{0.9}PbI_3$ and stirred 6 h at 60°C. The perovskite film was prepared by spin-coating at 1000 rpm for 10 s and 5000 rpm for 30 s, and 200 μL CB was dropped at 30 s during spinning, followed by annealing at 40 °C for 30 min and 100 °C for 15 min.

For $FAPbI_3$ film, 2 M precursor solution was prepared by dissolving PbI_2, FAI and 15 mol% MACl in DMSO and DMF (v:v = 1:4). The perovskite film was prepared by spin-coating at 1000 rpm for 5 s and 4000 rpm for 20 s, and 200 μL CB was dropped at 20 s during spinning, followed by annealing at 40 °C for 30 min in nitrogen atmosphere and 150 °C for 5 min and 100 °C for 10 min in ambient air.

For $MAPbI_3$ film, 1.5 M precursor solution was prepared by dissolving MAI and PbI_2 in mixed solvents of DMSO and DMF (v:v = 1:7) with a chemical formula of $MAPbI_3$. The perovskite film was prepared by spin-coating at 1000 rpm for 5 s and 4000 rpm for 20 s, and 120 μL CB was dropped at 20 s during spinning, followed by annealing at 40 °C for 30 min and 100 °C for 10 min.

For the preparation of fully covered and partially covered films, PTAA was used as the

HTL. Due to the hydrophobicity of PTAA, a partially covered film was obtained by spin-coating the perovskite precursor solution onto the PTAA-coated substrate. To achieve a fully covered film, the substrate was pre-rinsed with DMF before spin-coating the precursor solution. The spin-coating process and annealing temperature were consistent with those used for the preparation of the $Cs_{0.05}FA_{0.81}MA_{0.14}PbI_{2.85}Br_{0.15}$ film in solar cells.

Characterization

SEM image of the solar cell device was characterized by field emission scanning electron microscopy (FESEM, HITACHI S4800 and Helions G4 UC). Atomic force microscopy (AFM, Bruker MultiMode 8, Bruker Dimension Icon and Oxford instruments, MFP-3D) was used to probe the surface morphology, modulus, potential and conductivity of perovskite films. HR-TEM was performed using a ThermoFisher Talos F200X microscope at 200 kV. To minimize possible electron beam-induced artefacts, we used low-dose TEM imaging conditions, with an electron dose rate of ~10 e $Å^{-2}$ s^{-1}. Photoluminescence (PL) spectrum was acquired by QEPRO spectrophotometer in air at room temperature with the excitation wavelength of 532 nm. PL mapping of perovskite films was measured by a FLRM300 Time-Tech Spectra system. Time-resolved PL (TRPL) spectra were acquired using a Fluorolog-3-p spectrophotometer. Ultraviolet-visible (UV-vis) spectra of the perovskite were carried out on a Cary 500 UV-vis-NIR spectrophotometer. *J-V* curves of solar cells were measured under an AM 1.5G light simulator (Solar IV-150A, Zolix) calibrated to 100 mW cm^{-2} by a standard KG5-filtered Si reference cell. All devices were measured by a Keithley 2400 digital source meter with a scan rate of 0.15 V s^{-1}. The device active area was masked to be 0.0625 cm^2. Trap density of states (tDOS) of solar cells was derived from the frequency-dependent capacitance (C-f) and voltage-dependent capacitance (C-V), which were performed by an Agilent E4980A LCR meter. Transient photocurrent/photovoltage decays (TPV) of PSCs were collected on a digital storage oscilloscope (KEYSIGHT, DSOX3104T) with a nitrogen laser (337 nm, SRS NL100).

Electrochemical impedance spectra were measured using an electrochemical workstation (CHI760E) in the frequency range of 1.0 MHz and 1.0 Hz at 0.8 V under dark condition. Grazing incidence wide angle X-ray scattering (GIWAXS) was taken using Xeuss 2.0. The grazing-incidence angles for all films were 0.1°.

Computational calculations

The strain and stress of perovskite polycrystalline film were calculated using the finite element method (FEM). The model dimensions of the film were 1.5 μm × 1.5 μm, with an average grain size of ~300 nm and a GB width of 1 nm. Crystal expansion was modeled within the framework of thermoelasticity: the thermal expansion coefficients of the grains were from 0 to 0.001, 0.002, 0.003, 0.004 K^{-1}, corresponding crystal expansion from 0% to 0.4%. The GBs were assigned a fixed thermal expansion coefficient of 0 K^{-1}, and the temperature was increased by 1 K. Young's moduli were assumed to be 15 GPa for the grains and 1 GPa for the GBs, while Poisson's ratios were set to 0.33 for the grains and 0 for the GBs. Fixed boundary conditions were applied to the model. The linear continuum elastic theory was employed to calculate the stress and strain distributions by solving the following equation:

$$\sigma = \mathrm{D}\varepsilon \tag{1.1}$$

where σ is stress, ε is strain, and D is the stiffness matrix. Since isotropy of the elastic constants was considered in this model, the elastic constant tensor is represented as

$$D = \begin{pmatrix} C_{11} & C_{12} & C_{12} & 0 & 0 & 0 \\ C_{12} & C_{11} & C_{12} & 0 & 0 & 0 \\ C_{12} & C_{12} & C_{11} & 0 & 0 & 0 \\ 0 & 0 & 0 & \frac{C_{12}-C_{11}}{2} & 0 & 0 \\ 0 & 0 & 0 & 0 & \frac{C_{12}-C_{11}}{2} & 0 \\ 0 & 0 & 0 & 0 & 0 & \frac{C_{12}-C_{11}}{2} \end{pmatrix} \quad (1.2)$$

in which

$$C_{11} = \frac{E(1-\upsilon)}{(1+\upsilon)(1-2\upsilon)} \quad (1.3)$$

$$C_{12} = \frac{E\upsilon}{(1+\upsilon)(1-2\upsilon)} \quad (1.4)$$

where *E* and *v* are C_{11}Young's modulus and Poisson's rate for the materials given above.

First-principles calculations based on all spin-polarized density functional theory (DFT) were conducted using Vienna Ab initio Simulation Package (VASP) within the generalized gradient approximation (GGA) using the Perdew-Burke-Ernzerhof (PBE) formulation. We have chosen the projected augmented wave (PAW) potentials to describe the ionic cores and take valence electrons into account using a plane wave basis set with a kinetic energy cutoff of 450 eV. Partial occupancies of the Kohn−Sham orbitals were allowed using the Gaussian smearing method and a width of 0.05 eV. The electronic energy was considered self-consistent when the energy change was smaller than 10^{-5} eV. A geometry optimization was considered convergent when the energy change was smaller than 0.02 eV $Å^{-1}$. The vacuum spacing in a direction

perpendicular to the plane of the structure is 18 Å. The weak interaction was described by DFT+D3 method using empirical correction in Grimme's scheme.

The equilibrium crystal structure was then subject to compressive strain (0.2%, 0.4% or 0.6%) along the [001] crystallographic orientations. The formation of iodine vacancy defects was probed in a series of 4 structures for each value of strain (ε), with the defect energy calculated from equation 1:

$$E(\varepsilon) = E_{\varepsilon}(defect) + E(I) - E(bulk)$$

Where, $E\varepsilon$ (defect) and E(bulk) is the total energy of the strained and unstrained structure, and E(I) is the half energy in I_2.

The defect concentration at finite temperatures were calculated from equation 2:

$$n(\varepsilon) = e^{-\frac{E(\varepsilon)}{k_B T}}$$

Where, T is the temperature, k_B is the Boltzmann constant.

The structural formation energy (E_f) calculated from equation 3:

$$E_f = \frac{E_{tot} - N_C E_C - N_N E_N - N_H E_H - N_{Pb} E_{Pb} - N_I E_I}{N_C + N_N + N_H + N_{Pb} + N_I}$$

Where, E_{tot} is the total energy of the structure, N_i is the number of atoms, E_i is the energy of a single atom in a stable elemental state.

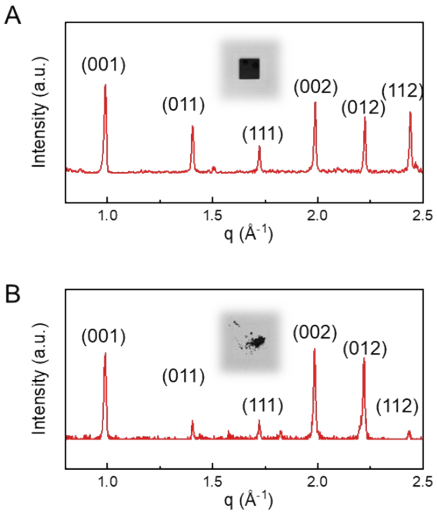

Figure S1. XRD spectra of ternary perovskite (A) film and (B) powder. The XRD peaks are almost overlapped in the samples, indicative negligible residual strain in the as-prepared films.

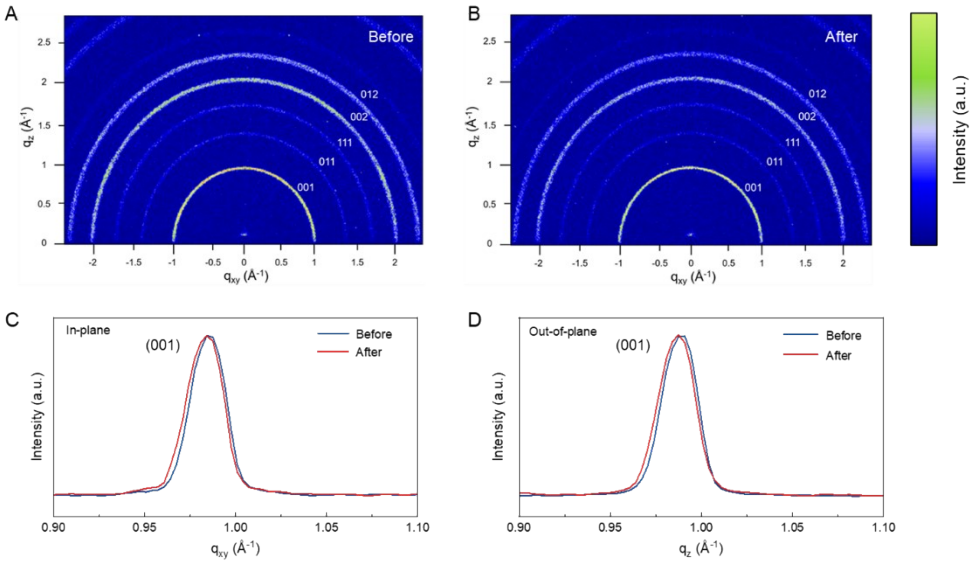

Figure S2. GIWAXS images of ternary perovskite films (A) before and (B) after light soaking. The 1D GIWAXS of ternary perovskite films derived from the corresponding GIWAXS patterns, (C) in-plane direction and (D) out-of-plane direction.

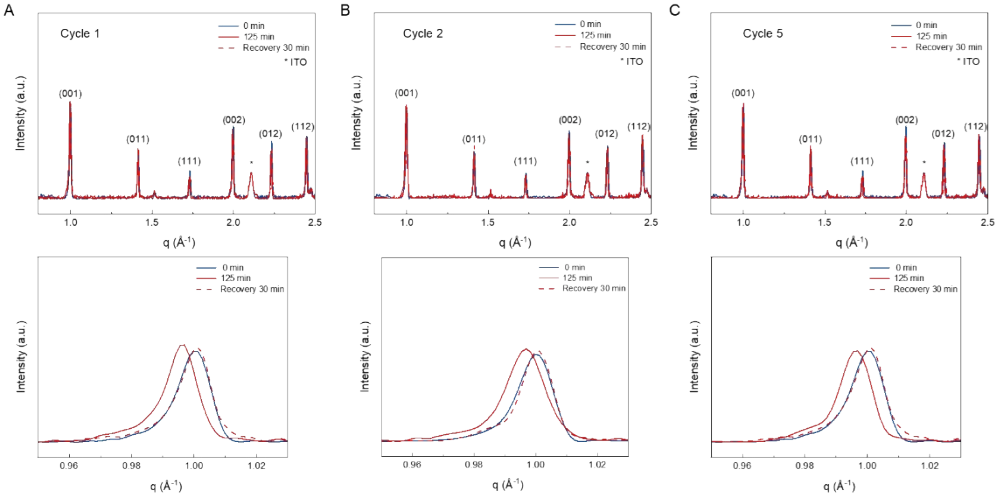

Figure S3. XRD spectra of ternary perovskite film at under alternating light and dark conditions.

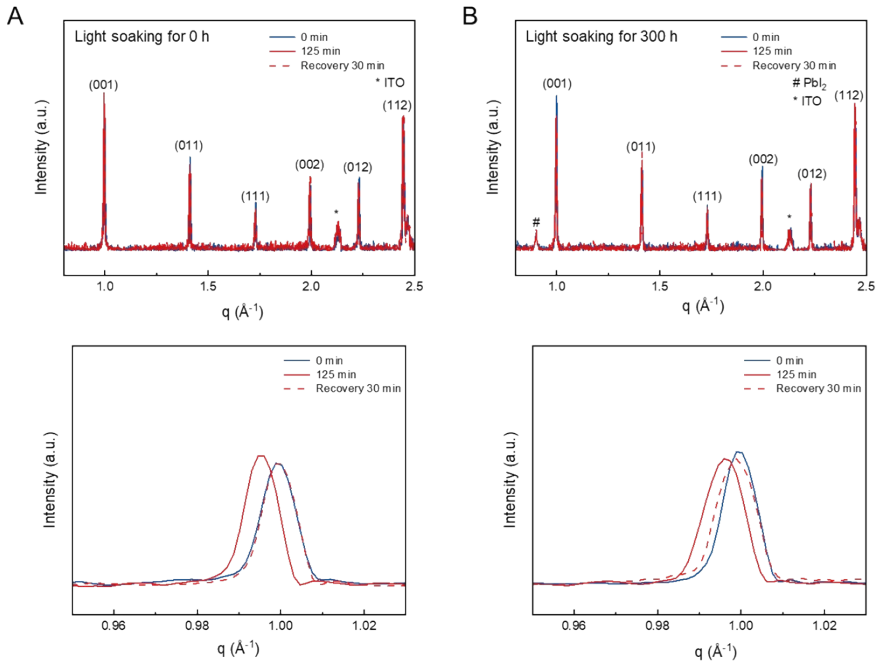

Figure S4. XRD spectra of ternary perovskite films (A) without and (B) with light soaking under one-sun illumination at 45 °C for 300 h. All films were subjected to one-sun illumination for 125 min and then dark condition to examine the lattice expansion and recovery behavior.

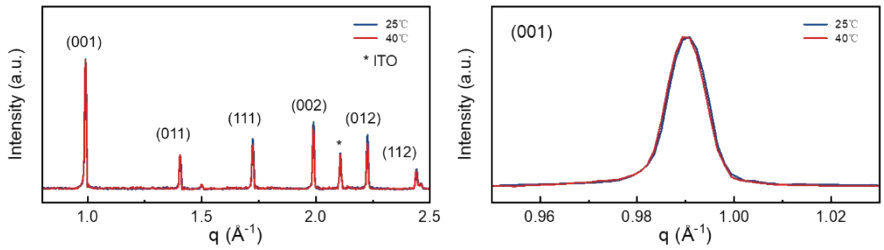

Figure S5. XRD spectra of ternary perovskite film at 25 °C and 40 °C. The increase in temperature resulted negligible lattice expansion.

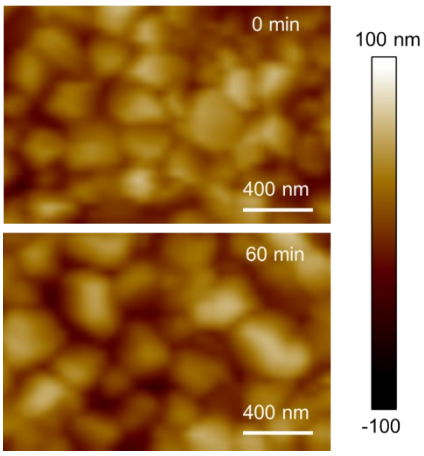

Figure S6. AFM images of ternary perovskite film before and after light soaking, corresponding DMT modulus maps of Figure 1D.

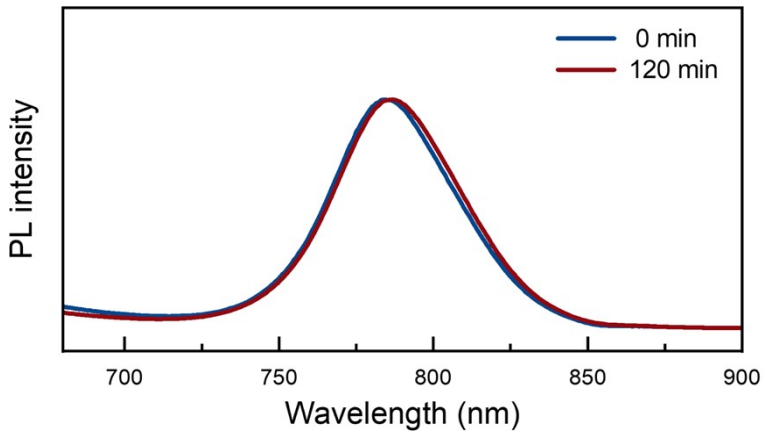

Figure S7. PL spectra of ternary perovskite film under a constant illumination for 120 min.

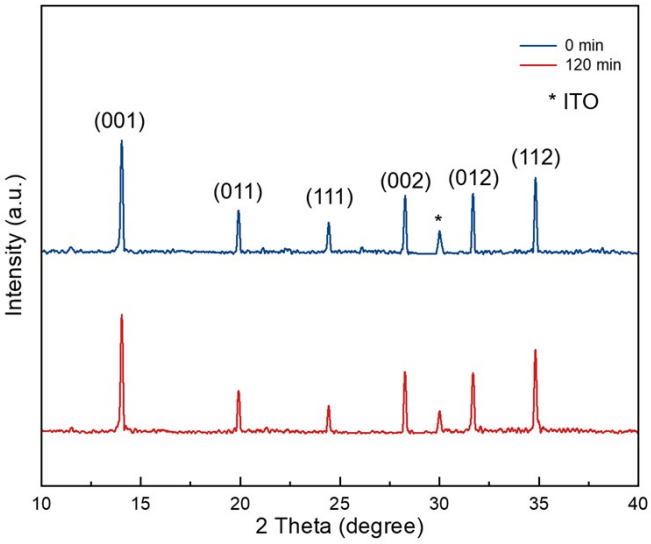

Figure S8. XRD spectra of ternary perovskite film under a constant illumination for 0 min and 120 min.

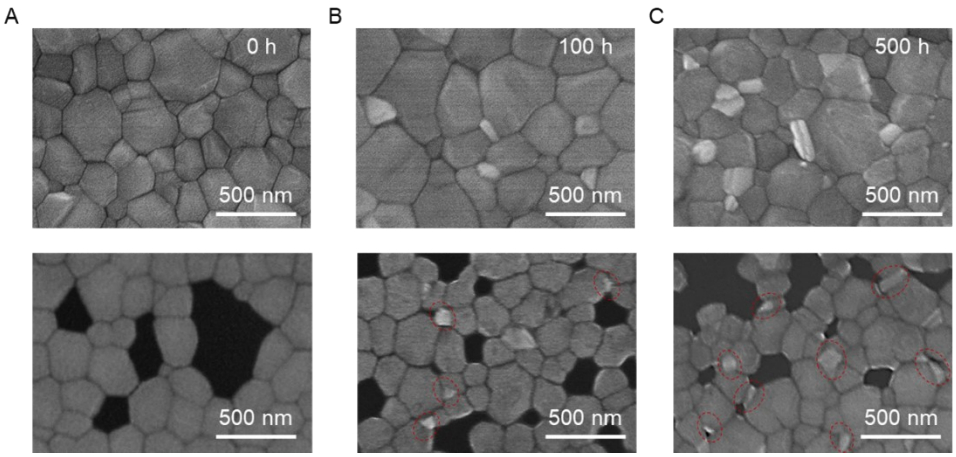

Figure S9. SEM images of the two types of perovskite films after light soaking for (A) 0 h, (B) 100 h, and (C) 500 h. The decomposition products of PbI_2 are primarily nucleated from contacted GB regions.

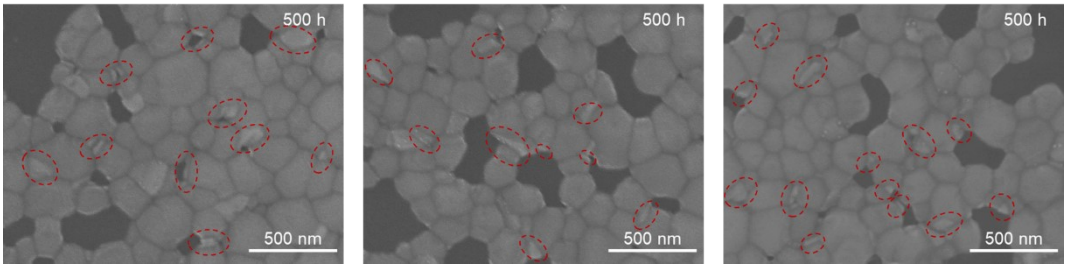

Figure S10. SEM images of semi-covered perovskite films after light soaking for 500 h.

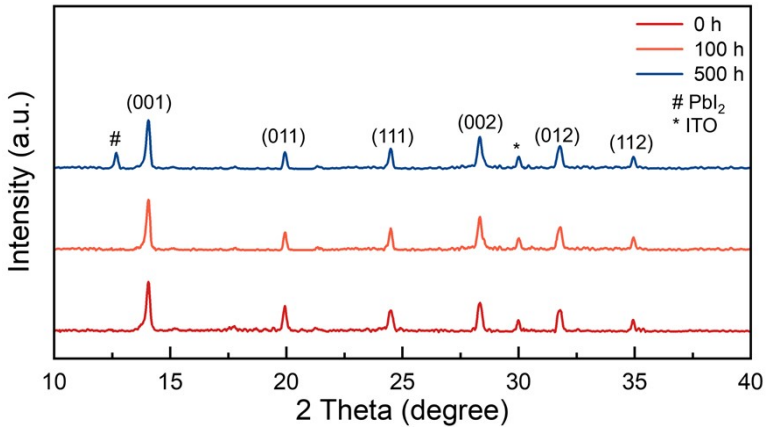

Figure S11. XRD spectra of a ternary perovskite film after different illumination times.

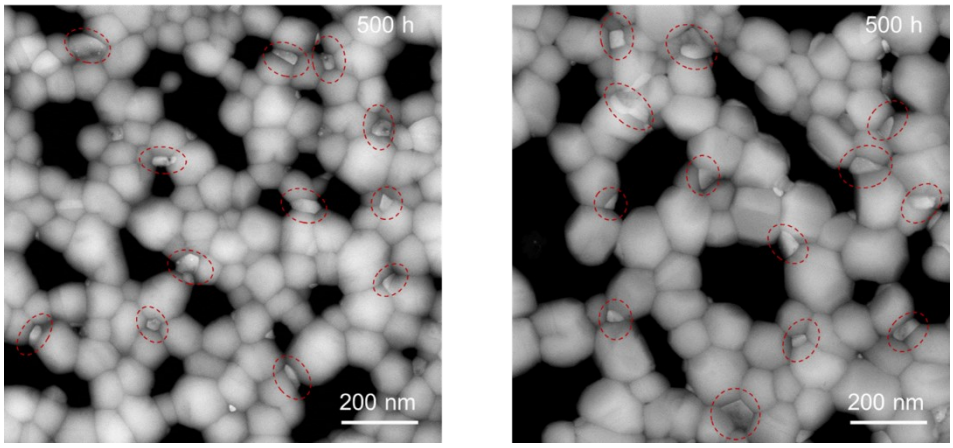

Figure S12. HAADF-STEM images of semi-covered perovskite films after light soaking for 500 h.

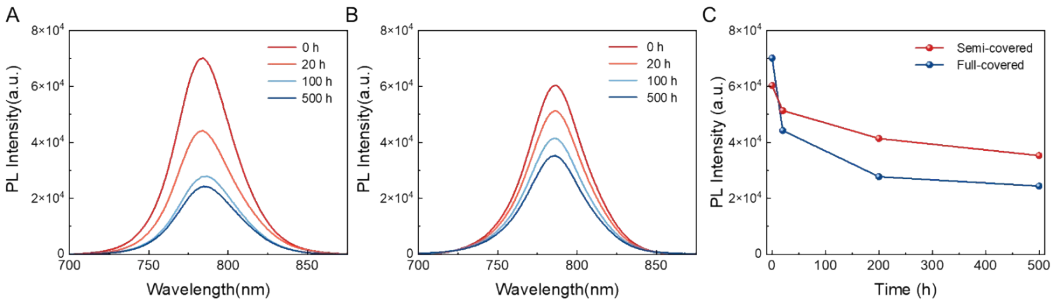

Figure S13. Steady-state PL spectra of (A) full-covered and (B) semi-covered ternary perovskite films. (C) Evolution of PL intensity of the perovskite films upon light illumination.

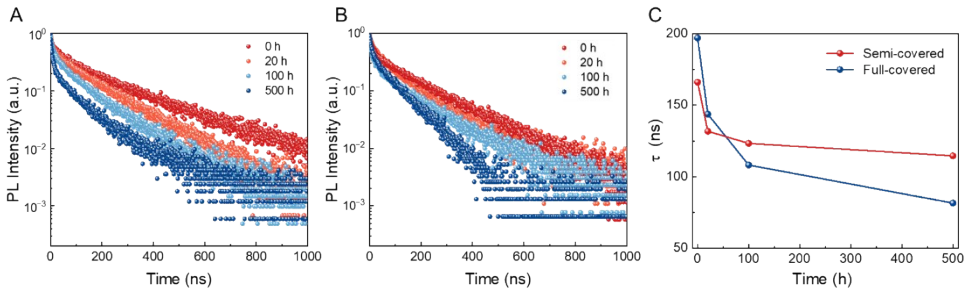

Figure S14. TRPL decay curves of (A) full-covered and (B) semi-covered ternary perovskite films. (C) Evolution of decay lifetime of the perovskite films upon light illumination.

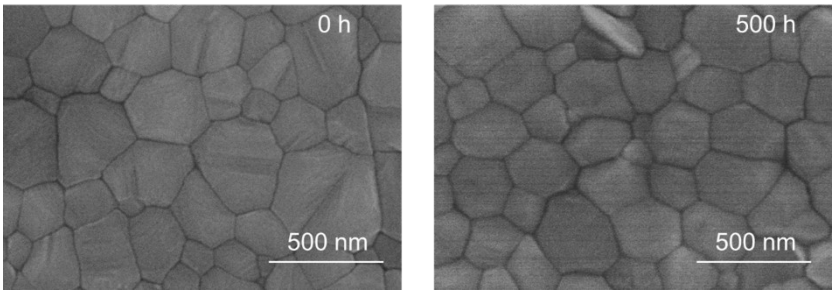

Figure S15. SEM images of ternary perovskite films on polydimethylsiloxane (PDMS) under various illumination times.

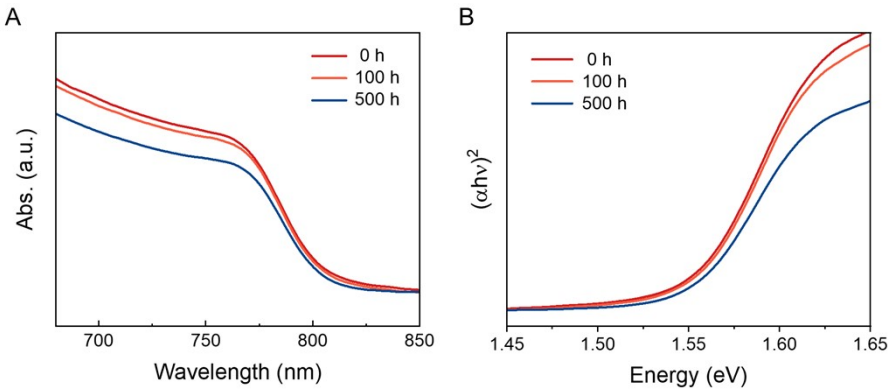

Figure S16. (A) Absorbance spectra and (B) corresponding Tauc plots of ternary perovskite films under various illumination times.

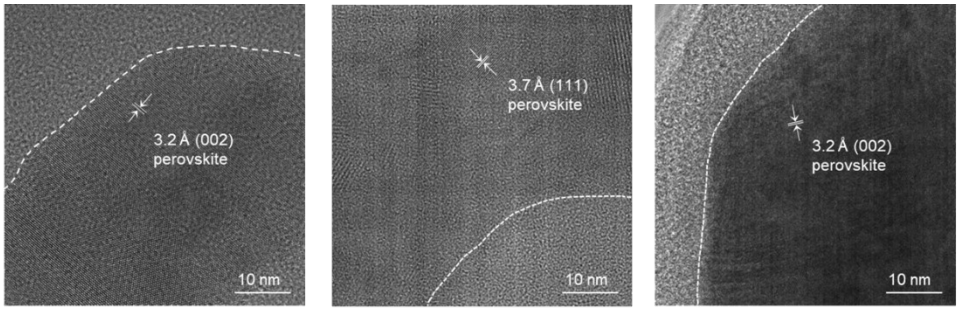

Figure S17. Typical HR-TEM images of the non-contact GBs under AM 1.5G illumination for 500 h. To address the limitations of TEM observations and to avoid any potential incidental conclusions, we provide additional comparisons between the two regions after prolonged illumination.

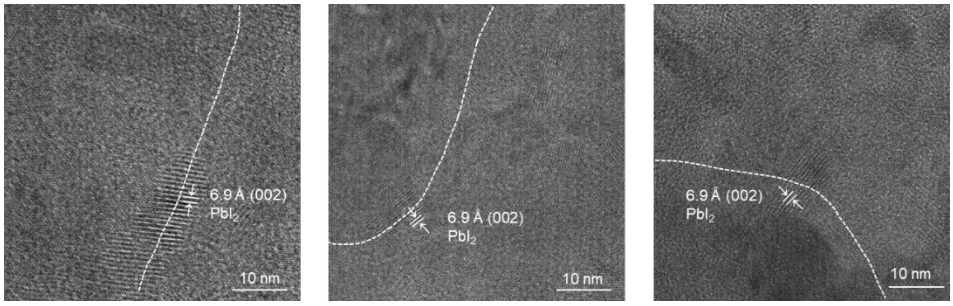

Figure S18. Typical HR-TEM images of the contacting GBs under AM 1.5G illumination for 500 h.

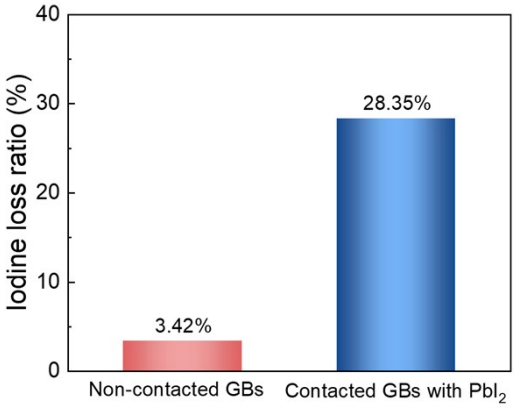

Figure S19. The comparison of iodine loss ratio between two types of GBs during illumination for 500 h.

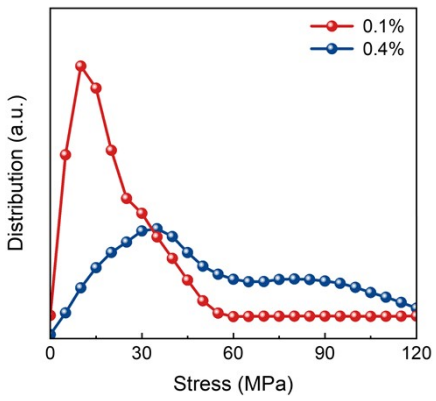

Figure S20. Statistics of stress extracted from the finite element simulation results. The emergence of additional peaks at high stress is derived from the GBs.

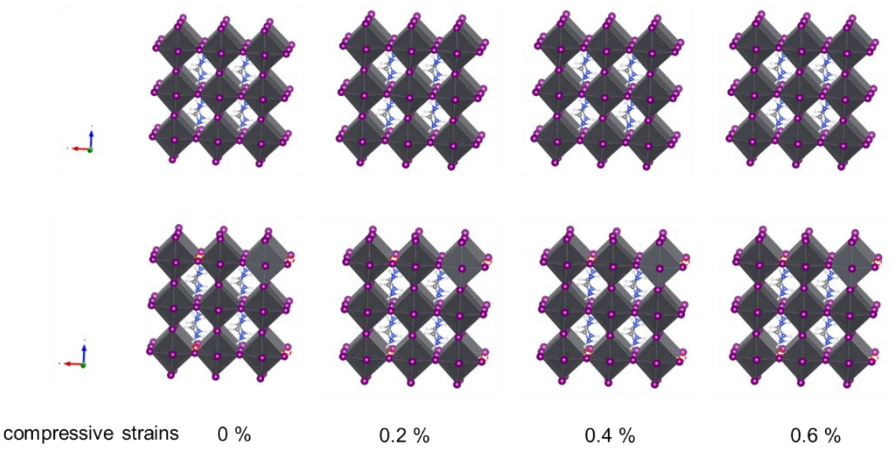

Figure S21. Structural models of cubic $FAPbI_3$ with and without iodine vacancy defects under various uniaxial compressive strains along [001] axis.

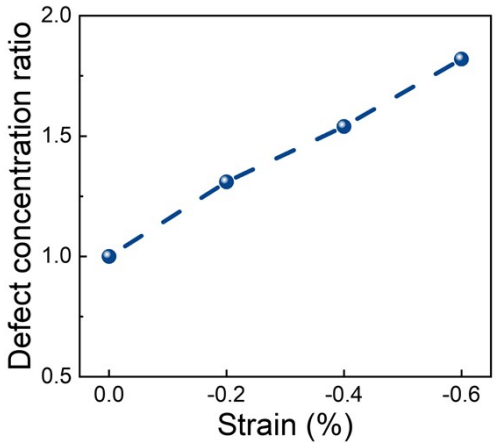

Figure S22. Calculated ratio of V_I^+ defect concentration of (001) strained perovskite crystals to unstrained one at 300 K.

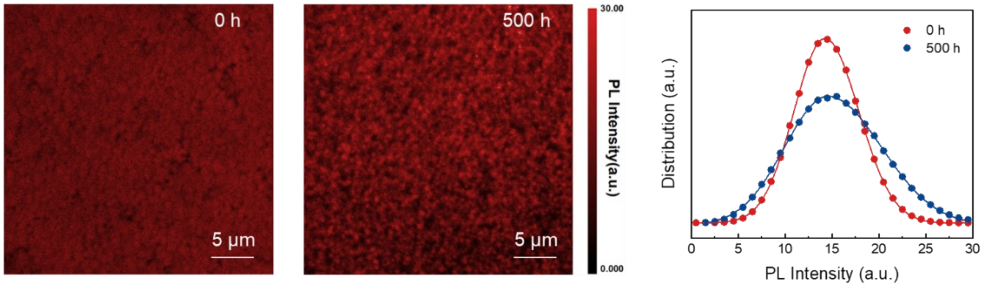

Figure S23. PL intensity mapping (left) and distribution (right) of the perovskite films before and after 500 h illumination.

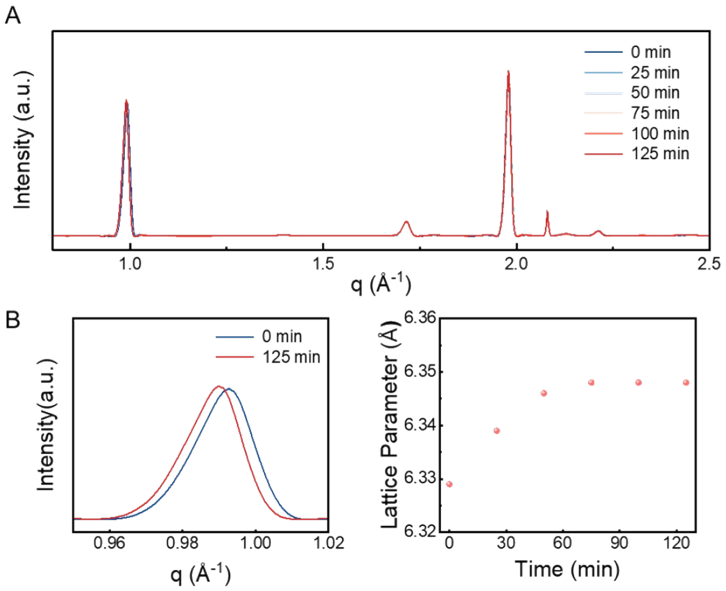

Figure S24. (A) In situ XRD spectra of $Cs_{0.1}FA_{0.9}PbI_3$ perovskite film under various illumination times. (B) Dependance of lattice parameter d values for the (001) crystal plane as a function of illumination time.

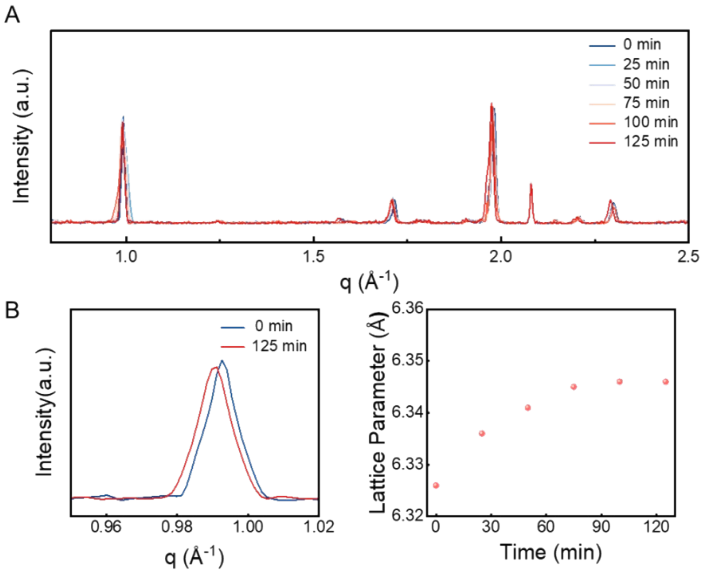

Figure S25. (A) In situ XRD spectra of $FAPbI_3$ perovskite film under various illumination times. (B) Dependance of lattice parameter d values for the (001) crystal plane as a function of illumination time.

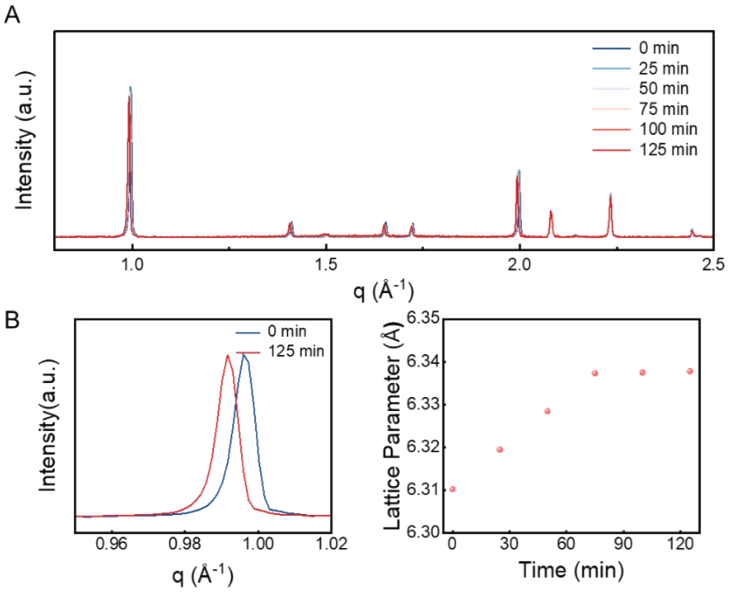

Figure S26. (A) In situ XRD spectra of $MAPbI_3$ perovskite film under various illumination times. (B) Dependance of lattice parameter d values for the (011) crystal plane as a function of illumination time

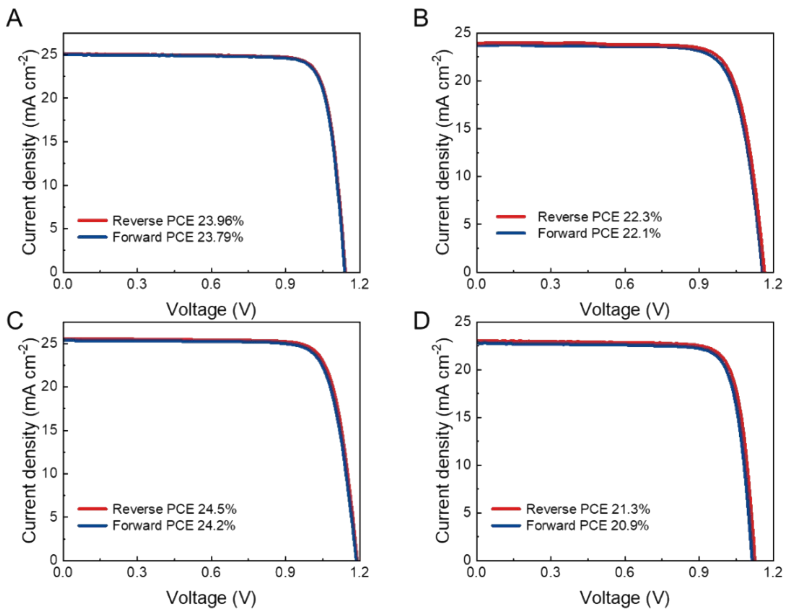

Figure S27. Initial *J-V* characteristics of the devices with different perovskite compositions: (A) $Cs_{0.05}FA_{0.81}MA_{0.14}PbI_{2.85}Br_{0.15}$, (B)$Cs_{0.1}FA_{0.9}PbI_3$, (C)$FAPbI_3$, and (D)$MAPbI_3$.

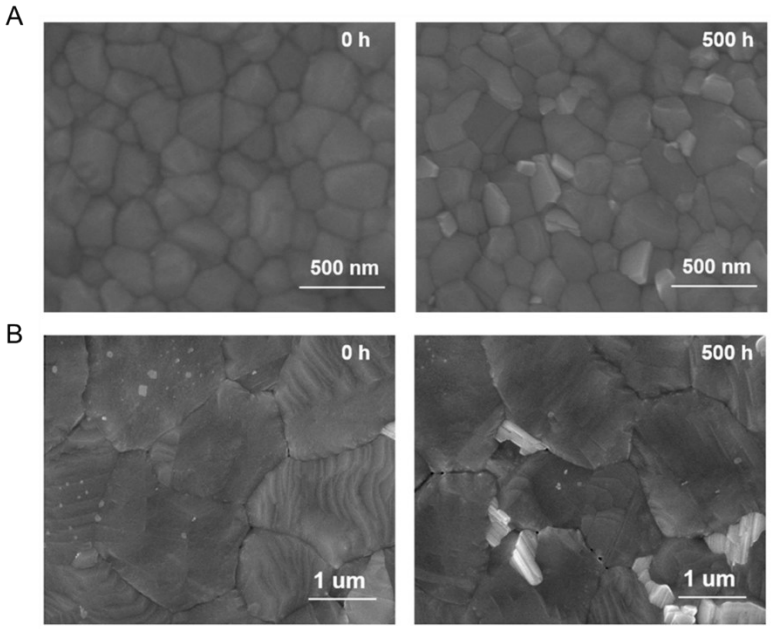

Figure S28. SEM images of (A) $MAPbI_3$ perovskite films and (B) $FAPbI_3$ perovskite films before and after 500 h illumination. The occurrence of lead iodide is concentrated at GBs for both samples.

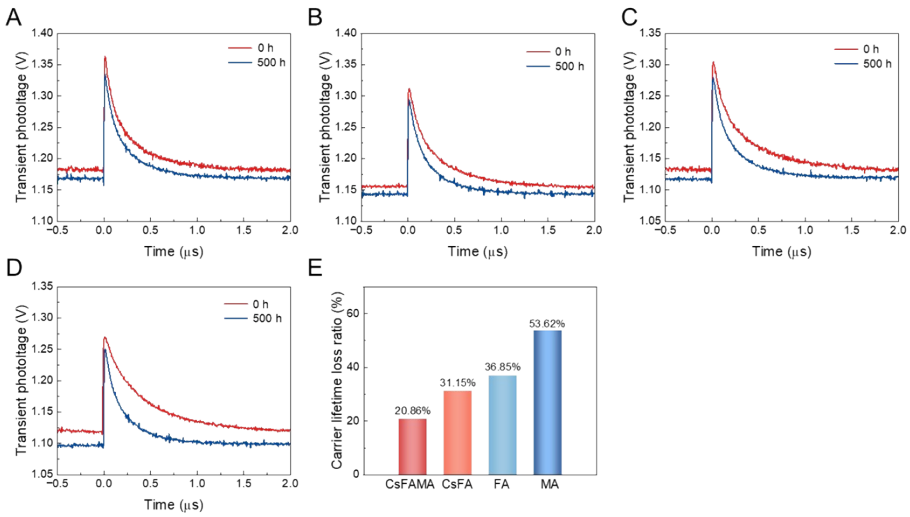

Figure S29. TPV decays of devices based on (A) $Cs_{0.05}FA_{0.81}MA_{0.14}PbI_{2.85}Br_{0.15}$, (B) $Cs_{0.1}FA_{0.9}PbI_3$, (C) $FAPbI_3$, and (D) $MAPbI_3$ before and after light soaking. (E) Loss ratio of carrier lifetimes of the four types of PSCs.

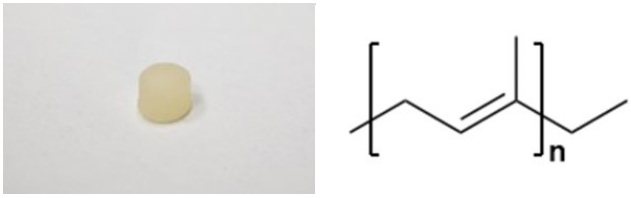

Figure S30. Photograph and molecular structure of TPI.

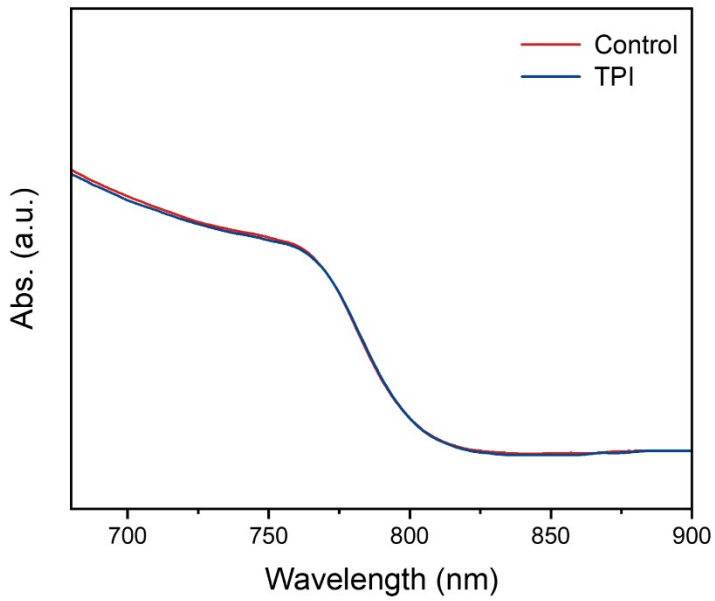

Figure S31. Absorbance spectra of ternary perovskite films with and without TPI.

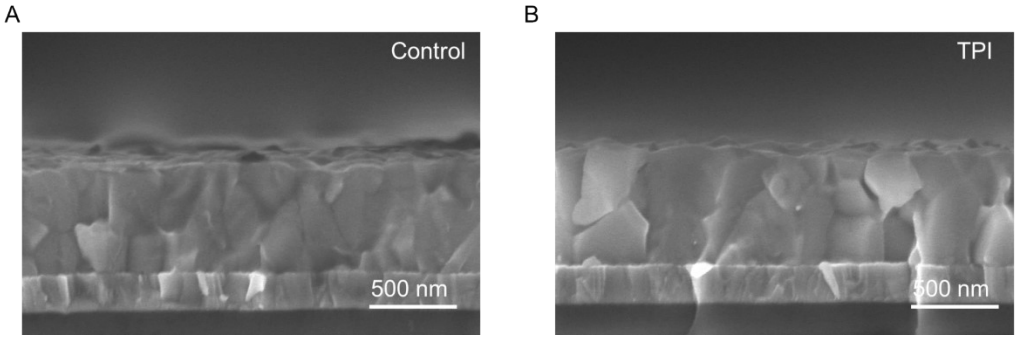

Figure S32. Cross-sectional SEM images of ternary perovskite films with and without TPI.

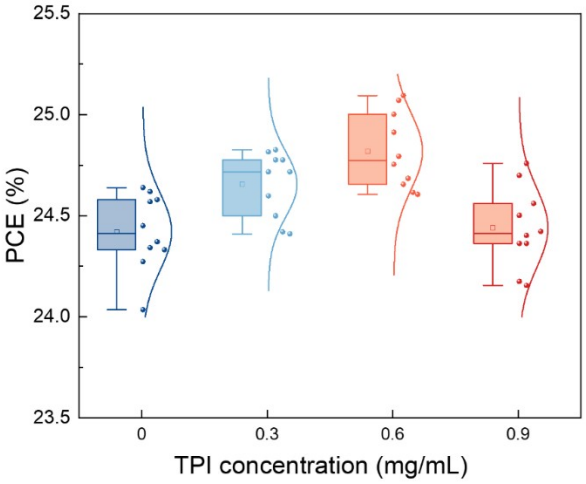

Figure S33. PCE distribution of different concentrations of TPI modified PSCs. The optimal TPI concentration for PSCs fabrication was determined to be 0.6 mg/mL.

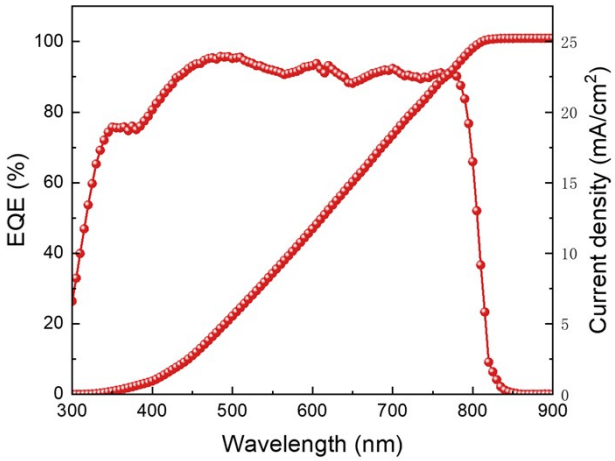

Figure S34. EQE spectra and integrated photocurrents of the TPI device. The $J_{SC,EQE}$ =25.22 mA/cm^2.

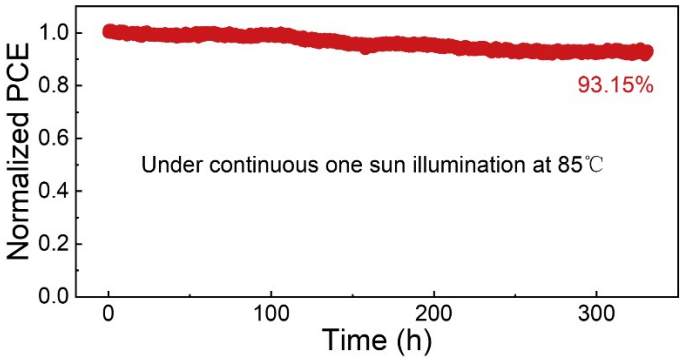

Figure S35. MPP tracking of an encapsulated PSC with TPI under constant one-sun illumination at 85 °C in air.

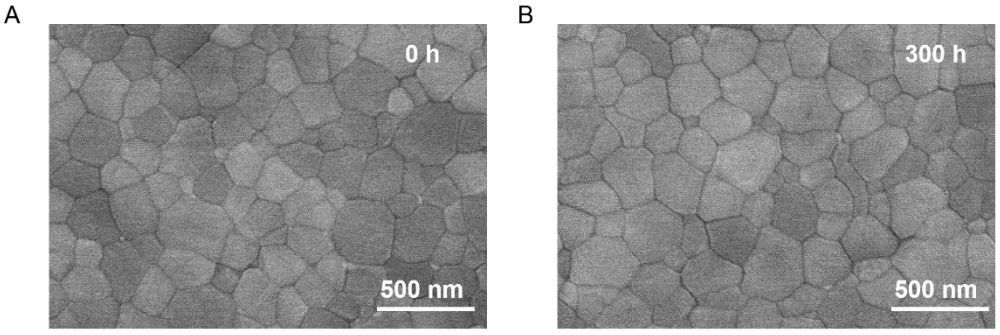

Figure S36. SEM images of ternary perovskite films containing TPI (A) before and (B) after light soaking for 300 h.

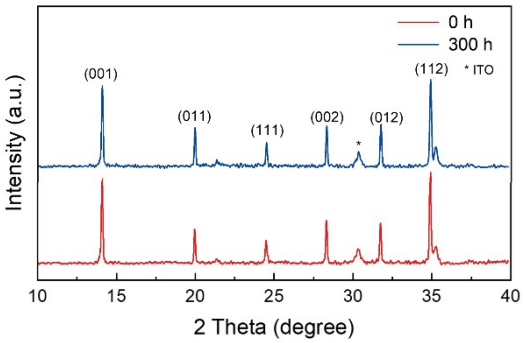

Figure S37. XRD spectra of ternary perovskite films containing TPI before and after light soaking for 300 h.

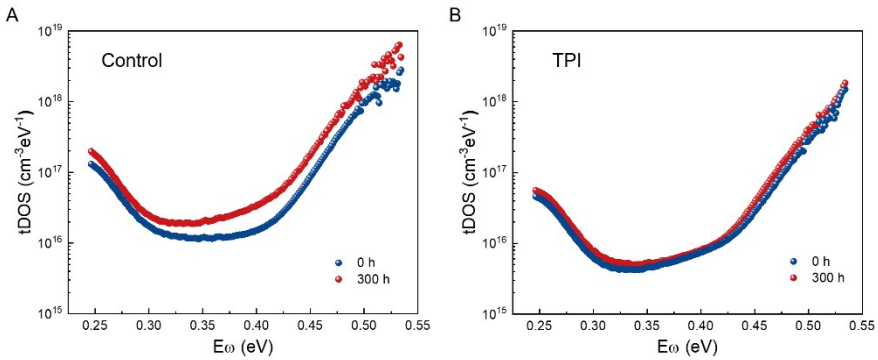

Figure S38. Trap density of states (tDOS) of (A) control and (B) TPI devices before and after light soaking for 300 h.

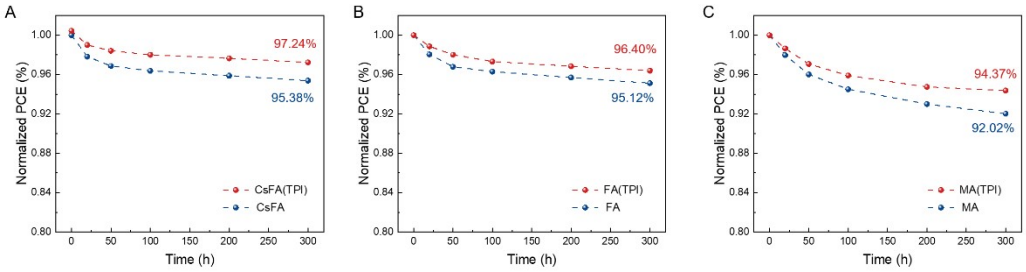

Figure S39. Light-soaking stability of PSCs based on (A) CsFA, (B) FA, and (C) MA perovskites under one-sun irradiation and open-circuit condition at 45 °C.

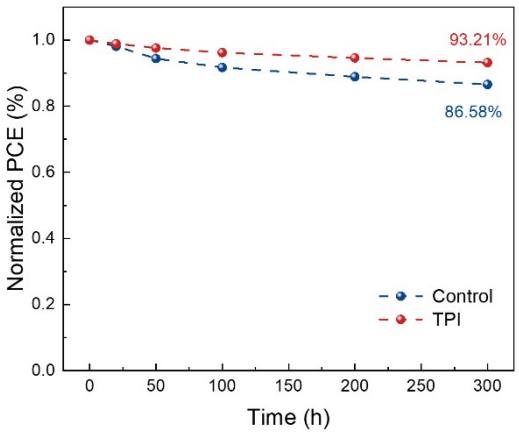

Figure S40. Light-soaking stability of PSCs based on wide bandgap perovskite under open-circuit condition at 45°C. The nominal chemical composition of perovskite is $Cs_{0.05}FA_{0.81}MA_{0.14}PbI_{2.4}Br_{0.6}$.

Table S1. The structural formation energies of the eight different structural models of cubic $FAPbI_3$.

	E_{tot} (eV)	E_{tot} (eV)	E_f (eV/atom)	E_f (eV/atom)
Strain (%)	Perfect bulk	Bulk with V_I^+	Perfect bulk	Bulk with V_I^+
0	-452.43803	-448.77813	-0.42411	-0.40798
-0.2%	-452.43085	-448.76206	-0.42403	-0.40781
-0.4%	-452.42123	-448.75266	-0.42393	-0.40771
-0.6%	-452.40709	-448.74255	-0.42378	-0.40760

Table S2. Average photovoltaic parameters of $Cs_{0.05}FA_{0.81}MA_{0.14}PbI_{2.85}Br_{0.15}$ (CsFAMA), $Cs_{0.1}FA_{0.9}PbI_3$ (CsFA), $FAPbI_3$ (FA), and $MAPbI_3$ (MA) PSCs in figure S26.

Sample[a]	V_{OC} (V)	J_{SC} (mA cm^{-2})	FF (%)	PCE (%)
CsFAMA	1.140	25.38	83.10	24.05
CsFA	1.163	23.80	79.85	22.1
FA	1.179	25.37	81.60	24.41
MA	1.123	22.90	82.24	21.15

[a] All parameters were collected from *J-V* curves of 15 pieces of devices.

Table S3. Average photovoltaic parameters of ternary PSCs with and without TPI.

Sample[a]	V_{OC} (V)	J_{SC} (mA cm^{-2})	FF (%)	PCE (%)
Without TPI	1.138	25.45	82.92	24.01
With TPI	1.145	25.89	83.45	24.73

[a] All parameters were collected from *J*-*V* curves of 15 pieces of devices.